Influence of reaction conditions on the properties of solution-processed Cu_2ZnSnS_4 nanocrystals

Yongtao Qu, Guillaume Zoppi, Robert W. Miles and Neil S. Beattie

Northumbria Photovoltaics Applications Group, Department of Physics and Electrical Engineering, Ellison Building, Northumbria University, Newcastle upon Tyne NE1 8ST, UK

E-mail: neil.beattie@northumbria.ac.uk.

Abstract. Cu_2ZnSnS_4 nanocrystals were fabricated by hot injection of sulphur into a solution of metallic precursors. By careful control of the reaction conditions it was possible to control the elemental composition of the nanocrystals such that they are suitable for earth abundant photovoltaic absorbers. When the reaction temperature increased from 195 ^oC to 240 ^oC the energy band gap of the nanocrystals decreased from 1.65 eV to 1.39 eV. This variation is explained by the identification of a mixed wurtzite-kesterite phase at lower reaction temperatures and secondary phase Cu_2SnS_3 at higher temperatures. Moreover, the existence of wurtzite structure depends critically on the reaction cooling rate. The reaction time was also found to have a strong effect on the nanocrystals which became increasingly copper poor and zinc rich as the reaction evolved. As the reaction time increase from 15 minutes to 60 minutes, the energy band gap increased from 1.42 eV to 1.84 eV. This variation is discussed in terms of the sample doping. The results demonstrate the importance of optimising the reaction conditions to produce high quality Cu_2ZnSnS_4 nanocrystals. PACS codes: 78.67.Bf, 61.46.-w, 81.07.-b, 81.05.Hd.

1. Introduction

Currently, absorber materials in thin-film photovoltaic (PV) cells, such as cadmium telluride (CdTe) and copper indium gallium selenide (CIGSe) have been used to produce solar cells with efficiencies > 20% [1]. However, the practical use of these materials for large scale PV applications may be restricted in the long term because they rely upon relatively scarce and expensive raw materials [2]. The quaternary compound copper zinc tin sulfide (CZTS) is one of the most promising alternative PV materials as it is composed of abundant and relatively cheap elements. In addition, CZTS has a near optimum direct energy band gap of ~1.5 eV and a large absorption coefficient of ~10^4 cm^{-1} (in the photon energy range greater than 1.2 eV) [3-6], minimizing the thickness of material needed to absorb the incident light and hence reducing material costs.

To obtain CZTS solar cells, evaporation and sputtering have been widely used for the deposition of CZTS thin films [7]. However, these high-vacuum deposition techniques generally require a large capital investment and considerable amount of energy to deposit thin films from the target sources. In contrast, solution-based deposition and processing could provide low-cost scalable routes to produce CZTS devices [8,9]. Noteworthy among the solution-based fabrication routes is the nanoparticle-based deposition of CZTS thin films from nanocrystal inks. CZTS nanocrystals inks can be spin-coated, sprayed, drop-casted, dip-coated or doctor bladed and provide an appealing alternative to the vacuum-based deposition approaches [10]. A non-vacuum deposition approach has recently achieved 9.0 % efficiency via the selenization of CZTS nanocrystals [11]. However, considering the detailed balance limit for CZTS, there is a large difference between the theoretical and experimental power conversion efficiencies. Secondary phases, such as copper tin sulfide (CTS), ZnS, $Cu_{2-x}S$, are considered as the main limiting factors on the electrical performance of CZTS [12]. Consequently, the controlled fabrication of CZTS nanocrystals is essential in order to achieve high efficiency CZTS nanocrystal-based solar cells.

Recently, CZTS nanocrystals have been prepared by several groups using the hot-injection method [3,4,6]. However, only the properties of CZTS nanocrystals fabricated at specific temperatures and times have been reported to date. There are few examples of systematic study of the structural and optical

properties of the CZTS nanocrystals as a function of the reaction conditions. In this work the CZTS nanocrystals were fabricated using a hot-injection method by tuning the reaction conditions. The results indicate that the crystal structure and composition are strongly influenced by the reaction conditions and play important roles in determining the optical properties of the CZTS nanocrystals.

2. Experimental procedure

2.1 Materials

Copper(II) acetylacetonate ($Cu(acac)_2$, 99.99%, Sigma Aldrich), zinc acetylacetonate ($Zn(acac)_2$, 99.995%, Sigma Aldrich), and tin(IV) bis(acetylacetonate) dichloride ($Sn(acac)_2Cl_2$, 98%, Sigma Aldrich), elemental sulphur (S, 99.98%, Sigma Aldrich) and oleylamine (OLA, technical grade, Sigma Aldrich) were all purchased and used as received. Toluene and isopropanol (IPA) were analytical grade and supplied from Fisher Scientific.

2.2 Nanocrystal Synthesis

CZTS nanocrytals were fabricated by the commonly reported hot-injection method involving the combination of metal salt precursors and sulphur dissolved in OLA. In order to identify the metal composition required to achieve high efficiency solar cells, the efficiencies of CZTSSe thin film devices were summarized on the ternary diagram shown in figure 1. To the best of our knowledge, the solar cells with the high conversion efficiencies exist in the Cu-poor and Zn-rich region but only a relatively narrow range of Cu/(Zn+Sn) = 0.75-0.85 and Zn/Sn = 1.05-1.25 as indicated by the dark hexagon on the figure. In this work, the precursor molar ratios were chosen to be Cu/(Zn + Sn) = 0.79 and Zn/Sn = 1.27. These were achieved by adding 1.34 mmol of $Cu(acac)_2$, 0.95 mmol of $Zn(acac)_2$, 0.75 mmol of $Sn(acac)_2Cl_2$, and 10 ml of OLA to a three-neck flask connected to a Schlenk line. After purging the reaction mixture with nitrogen, the temperature was increased to the reaction temperature where 3 ml of 1M sulphur-OLA solution was injected into the mixture. After injection, the reaction solution was held at a given temperature to allow the growth of the nanocrystals. Temperature-dependent experiments were performed

by setting the reaction temperature to 195, 210, 225 and 240 ^{o}C for a fixed reaction time of 30 min. Time-dependent experiments were performed by setting the time to 15, 30, 45 and 60 min at a fixed temperature of 225 ^{o}C.

After the reaction, 5 ml of toluene and 40 ml of IPA were added into the reaction mixture and the nanocrystals were collected using a centrifuge (separated into two 50 ml centrifuge tubes). After centrifuging at 8450 rpm for 10 minutes, the supernatant containing unreacted precursor and byproducts were discarded. The CZTS nanocrystals were then washed two times with toluene and IPA. Before storing the nanocrystal ink in a glass vial, a size selection process was performed to remove large particles and agglomerates by centrifuging at 7000 rpm for 3 min.

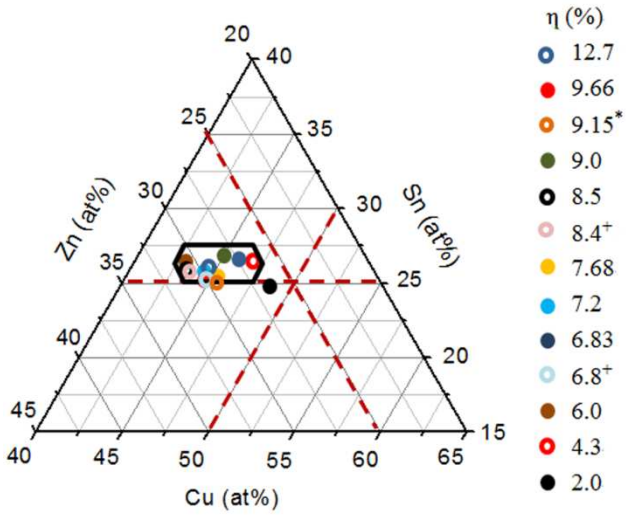

Figure 1. Efficiency map of CZTSSe thin film devices on the ternary phase diagram. The most common compositional ranges suitable for high efficiency photovoltaic devices are indicated by the dark hexagon. The absorber of the devices indexed with asterisk and cross are pure CZTSe and CZTS, respectively. References and process details are given in table S1.

2.3 Characterization

Transmission electron microscopy (TEM) observations were carried out on a JEOL JEM-2100F with an emission voltage of 200 kV. Samples were prepared by dropping a dilute toluene solution (~0.05 mg/ml) onto 200 mesh carbon coated Cu grids.

Atomic force microscopy (AFM) images were taken using a Veeco Nanoscope multimode system. Thin films of CZTS were deposited by spin-coating onto the soda-lime glass (SLG) substrate at 4000 rpm for 30 s.

The structure of the CZTS nanocrystals was examined using X-ray diffraction (XRD) carried out with a Siemens D-5000 diffractometer using a Cu K_α radiation source (λ=0.15406 nm) with step size of 0.02°. During scanning mode, the instrument was operated at 40 kV and 40 mA. Crystal sizing from XRD was performed using Scherrer analysis with a shape factor of 0.89 applied to the (112) reflection. Peak fitting was peformed using a Lorentzian function to study the full width at half maximum (FWHM) of peak (112). The (112) and (220) peaks were used for calculating the lattice parameters. For XRD analysis, 0.5 ml of CZTS inks (~10 mg/ml) was drop casted onto a 10×15 mm SLG substrate and dried in air overnight.

Energy dispersive X-ray spectroscopy (EDS) was performed in a FEI Quanta 200 scanning electron microscope (SEM) at 20 kV over ten 20 × 20 μm areas and averaged. K_α X-ray emission lines for Cu, Zn, S and L_α for Sn were used for quantification.

UV-VIS-NIR absorbance was obtained from 360-1600 nm using a Shimadzu SolidSpec 3700 spectrophotometer. All solutions were prepared with an absorbance of 0.020 ± 0.005 (after background correction) at 1600 nm in toluene.

Raman spectra were measured with a Renishaw 2000 system with a 514 nm excitation source.

3. Results and discussion

3.1 Control sample prepared at 225 ^oC for 30 min

Figure 2 (a) shows a low-magnification TEM image of the control sample prepared at 225 ^oC for 30 min. It can be seen that the CZTS nanocrystals have an irregular spherical shape and are slightly polydispersed with most of the nanocrystals having diameters in the range 10-25 nm. A high magnification TEM image of a CZTS nanocrystal is shown in figure 2 (b), which shows good crystallinity

of the nanocrystals. The interplanar spacing is measured to be 0.31 nm, which corresponds to the (112) planes in a kesterite structure [6].

The XRD pattern of a typical sample prepared at 225 ^{o}C for 30 min is shown in figure 2 (c). The peaks of as-synthesized CZTS nanocrystals were indexed to tetragonal CZTS (PDF 026-0575). The major XRD diffraction peaks appeared at about 28.5°, 47.5°, 56.3° can be attributed to the (112), (220), (312) planes of kesterite CZTS, respectively. The lattice parameters calculated for the CZTS nanocrystals were 5.410 Å and 10.843 Å for a and c, respectively. The lattice spacing of (112) is calculated to be 0.31 nm which matches well with the lattice spacing measured from high magnification TEM.

The diffraction patterns of stoichiometric tetragonal Cu_2SnS_3 (JCPDS 1-089-4714) and cubic ZnS (JCPDS 5-0566) have very similar lattice parameters to CZTS [3]. To rule out the possibility that binary and ternary compounds exist in the samples, Raman spectroscopy was used to confirm the structure of the control sample. This is shown in figure 2 (d). The peak located at 329 cm^{-1} is close to the reported values of the characteristic peak of CZTS (325-339 cm^{-1}) [12-19]. This peak is somewhat asymmetrical however characteristic peaks from $Cu_{2-x}S$ (475 cm^{-1}), Cu_2SnS_3 (298 cm^{-1}), Cu_3SnS_4 (318 cm^{-1}) and ZnS (355 cm^{-1}) were not observed [13]. The main band at 329 cm^{-1} is thought to be the A_1 mode of kesterite CZTS shifted downwards from 338 cm^{-1} due to the cation sublattice disorder for non-stoichiometry CZTS material [20].

Elemental analysis was performed on the samples using EDS are given in table 1. The average composition of the as-synthesized CZTS nanocrystals prepared at 225 ^{o}C for 30 min was $Cu_{1.72\pm0.02}Zn_{1.13\pm0.02}Sn_{0.96\pm0.01}S_{4\pm0.06}$ with a Cu/(Sn+Zn) ratio of 0.83 and a Zn/Sn ratio of 1.18. A quasi-ternary composition diagram of the nanocrystals is presented in Figure 3. The average composition of the control sample is copper-poor and zinc-rich, falling in the region for high performance solar cells as summarized in figure 1.

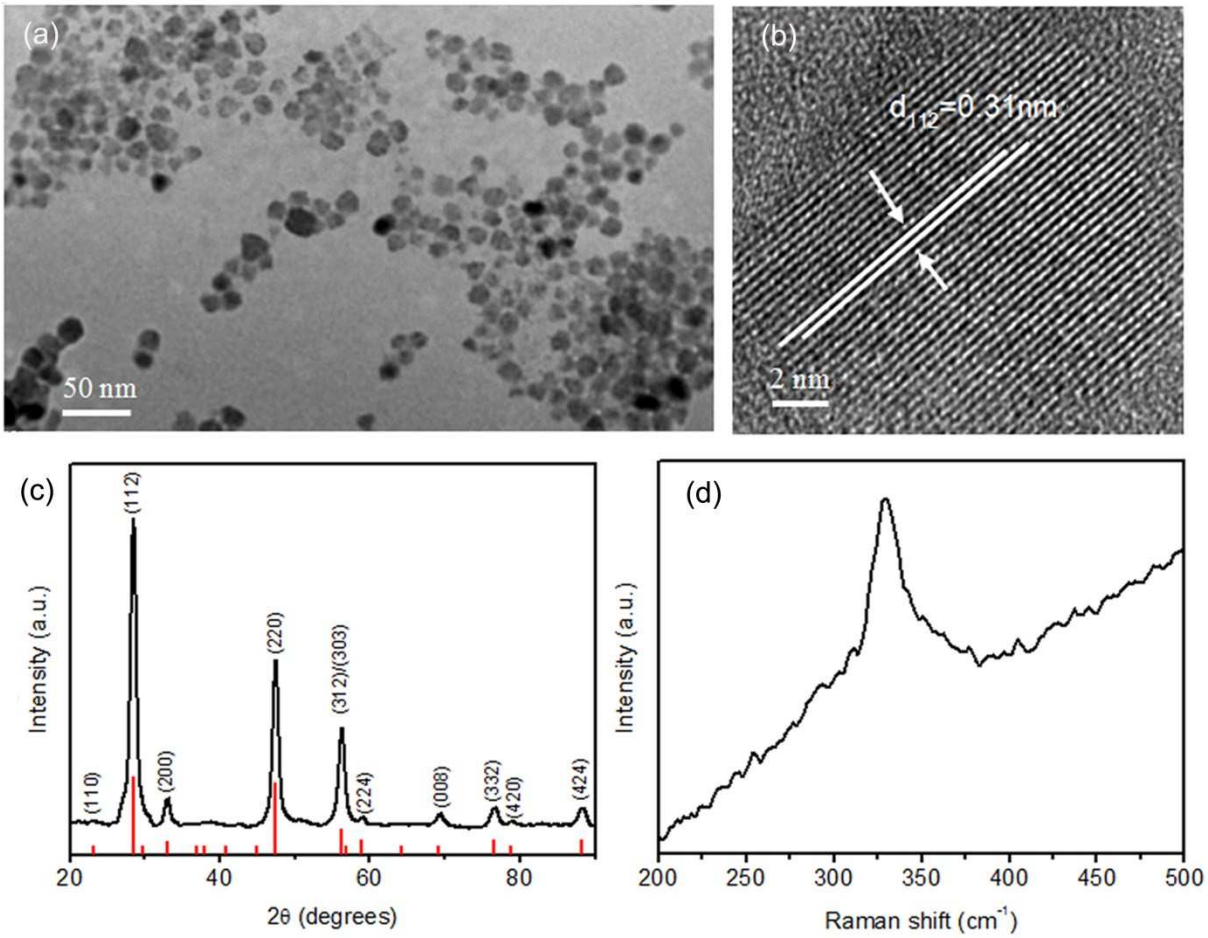

Figure 2. TEM images of CZTS nanocrystals at (a) low and (b) high magnification. (c) XRD pattern of as-synthesized CZTS nanocrystals compared to the reference pattern for kesterite CZTS (PDF 026-0575) and (d) Raman spectrum of CZTS nanocrystals.

Table 1. Elemental ratios of CZTS nanocrystals fabricated at different temperatures according to EDS measurements.

Temperature (^{o}C)	Cu/Zn/Sn/S	Cu/(Zn+Sn)	Zn/Sn
195	1.62/1.01/0.98/4	0.81	1.02
210	1.83/1.23/1.08/4	0.80	1.14
225	1.72/1.13/0.96/4	0.83	1.18
240	1.57/1.21/0.87/4	0.75	1.39

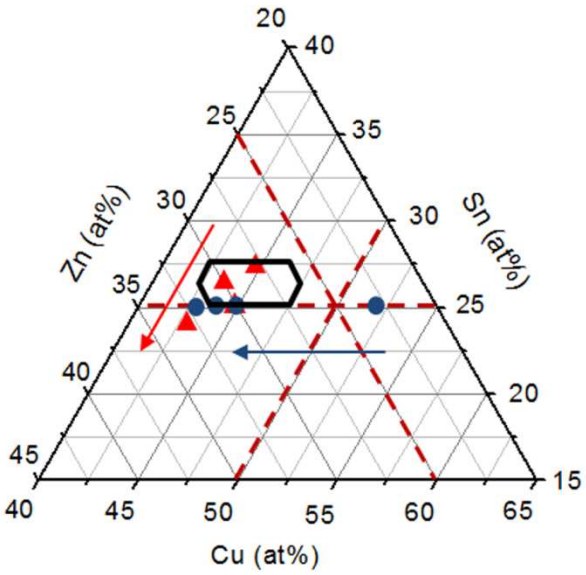

Figure 3. Quasi-ternary diagram based on the atomic percentage of Cu, Sn, and Zn in the nanocrystals. The red triangles show the compositions of nanocrystals fabricated at different temperatures and the red arrow points the direction of increasing temperature. The blue dots show the compositions of nanocrystals prepared at different times and the blue arrow indicates the direction of increasing time. The intersection of the dashed lines shows the stoichiometric point of CZTS. The highest efficiency CZTS-based PV devices lie inside the region indicated by the dark hexagon.

3.2 Influence of reaction temperature

The XRD patterns of the CZTS nanocrystals prepared at different temperatures (195-240 ^{o}C) are shown in figure 4 (a). The major diffraction peaks of all samples can be indexed to kesterite phase (PDF 026-0575). As shown in table 2, the intensity of the (112) and (220) diffraction peaks increases gradually with increasing reaction temperature, indicating the improvement of the crystallinity. The crystal size determined using the Scherrer equation was found to increase from 4.4 nm for 195 ^{o}C to 11.5 nm for 240 ^{o}C as shown in table 2. This was consistent with AFM images (figure S1) which exhibited the same trend toward large grains with increasing temperature. The average grain sizes (as determined from AFM) of CZTS nanocrystals prepared at different temperatures are given in figure 4 (c). It can be seen that the

grain size of CZTS nanoparticles increased from 14 nm for 195 °C to 20 nm for 240 °C. At higher temperatures, the ions have a greater reactivity, which facilitates the growth of the nanocrystals.

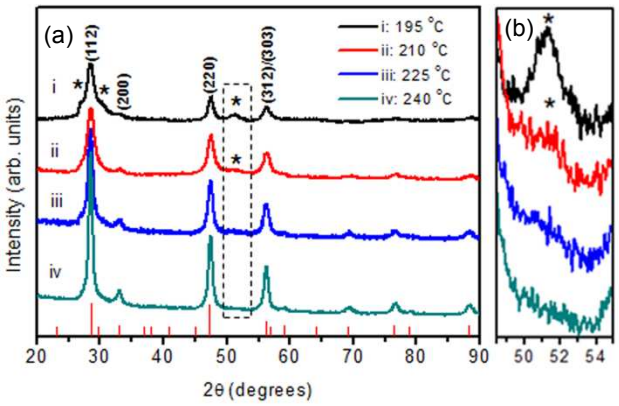

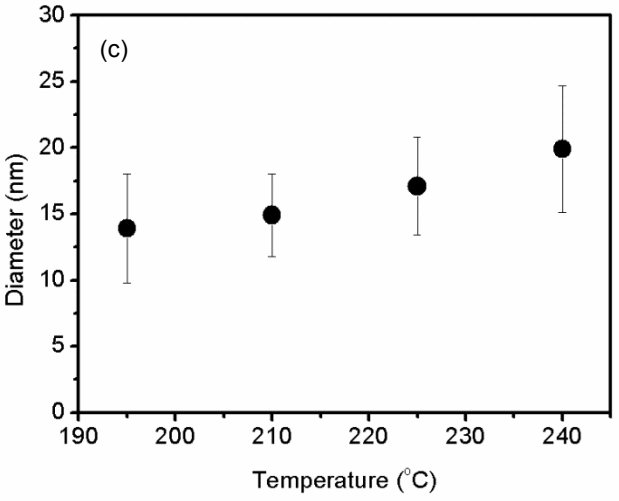

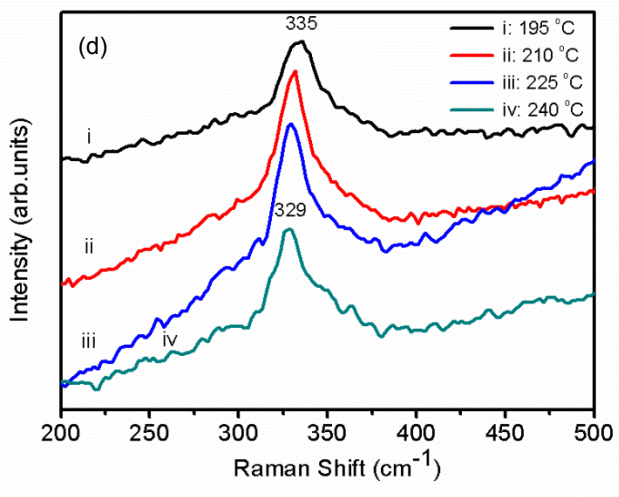

Figure 4. (a) X-ray diffraction patterns, (b) enlarged picture of dashed rectangle in (a), (c) average grain sizes and (d) Raman spectra and of CZTS nanocrystals prepared at a fixed reaction time of 30 minutes for different temperatures. The red lines in (a) are the reference XRD pattern of CZTS (PDF 026-0575). Diffraction patterns and Raman spectra are off-set for better visibility. The Raman spectra were smoothed using a Savitzky-Golay method.

As shown in figure 3, nanoparticles fabricated at 195, 210, and 225 ^{o}C fall in the composition region suitable for high efficiency solar cells. In addition, as the reaction temperature increased from 195 to 240 ^{o}C, the nanocrystals become richer in zinc and poorer in tin. From a kinetics viewpoint, increasing the reaction temperature increases the reactivity of all cations. However, it appears that the relative increase in reactivity of Zn^{2+} is larger than that of Sn^{4+}, which results in more Zn being incorporated into the lattice making the nanocrystals richer in zinc and poorer in tin at higher temperature.

Table 2. XRD peak intensity, calculated crystal domain size, characteristic Raman peak, and band gap energy of CZTS nanocrystals fabricated at different temperatures.

Sample	Peak intensity (a.u.)		Crystal size	Raman peak	Band gap
	(112)	(220)	(nm)	(cm^{-1})	(eV)
195 ^{o}C	1070	483	4.4	335	1.65
210 ^{o}C	1346	785	6.3	332	1.61
225 ^{o}C	1699	954	10.0	329	1.52
240 ^{o}C	3127	1543	11.5	329	1.39

In addition to the main peaks, the CZTS nanocrystals prepared at 195 ^{o}C also exhibit three weak diffraction peaks marked by asterisks shown in figure 4 (a). The sample prepared at 210 ^{o}C exhibits one of these three diffraction peaks around 51° as shown in figure 4 (b). These peaks can be indexed to either wurtzite CZTS [14,15,21,22] or wurtzite ZnS [23,24]. However, as shown in figure 4 (c), there is only the characteristic peak of CZTS in the Raman data located around 330 cm^{-1} and this rules out the existence of ZnS. First-principle calculations suggest that wurtzite CZTS is unstable and prone to transit to the more stable kesterite CZTS phase [15,23]. However, some metastable wurtzite CZTS may not have enough time to finish this transition before the temperature cooled down from lower reaction temperature to 70 ^{o}C

when toluene was added to quench the reaction. To verify this assumption an experiment was performed in which the reaction mixture was stirred at 225 °C for 30 min and then cooled rapidly in ice-water until it reached to 70 ^{o}C where toluene was added to quench the reaction. The crystal structure of the sample was then studied using XRD as shown in figure 5 (a). Compared with the control sample that cooled down naturally, XRD peaks belonging to wurtzite CZTS are evident. The relatively short transition time after the reaction leads to some metastable wurtzite CZTS in the sample. This observation indicates that the cooling mode plays an important role and will have a potential impact on a pure phase CZTS fabrication.

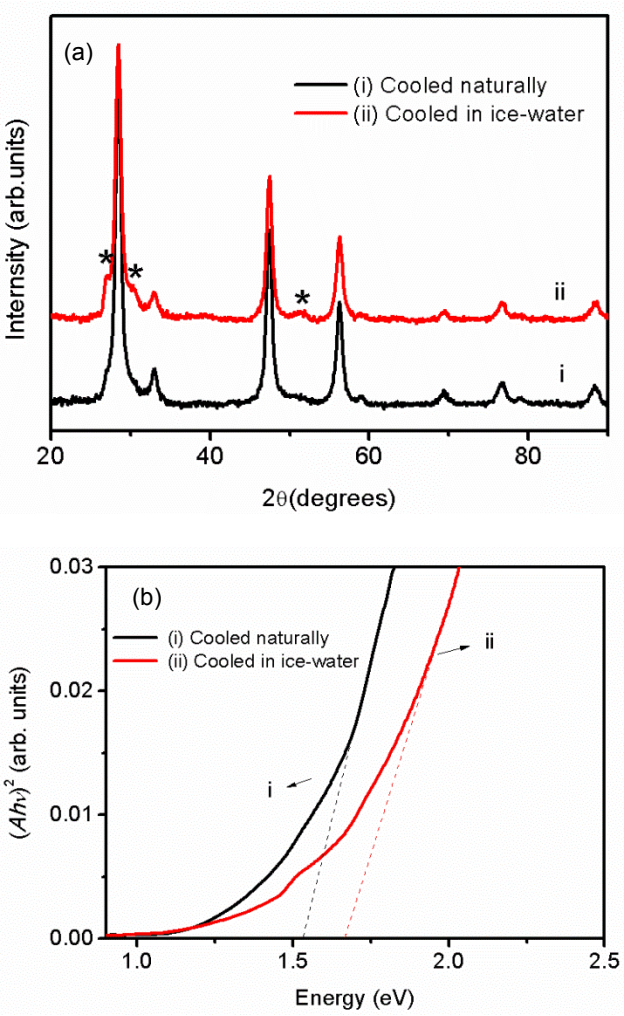

Figure 5. (a) XRD pattern and (b) dependence of $(Ahv)^2$ on hv of the CZTS nanocrystals prepared at 225 ^{o}C for 30 min. After the reaction, the reaction vessel was cooled down to 70 ^{o}C (i) naturally and (ii) in an ice-water bath. The peaks belonging to wurtzite CZTS are indexed using asterisks.

The change in the Raman spectra as a function of temperature shown in figure 4(c) correlates with the XRD data. At 195 ^{o}C, a broad peak characteristic of CZTS was observed at 335 cm^{-1}. This is likely to be a result of a mixed kesterite and wurtzite atomic arrangement [12]. Increasing the temperature caused the peak to downshift as the kesterite component becomes more dominant. Similar to the XRD, no further change was observed ≥ 225 ^{o}C as the characteristic CZTS peak remained at 329 cm^{-1}. At 240 ^{o}C however, the characteristic Raman peak was observed to broaden relative to the lower temperature. Peak fitting (figure S2) allows deconvolution of the data into peaks at 295 cm^{-1} and 359 cm^{-1} which matches well with tetragonal Cu_2SnS_3 (CTS) at 297 and 352 cm^{-1} [13].

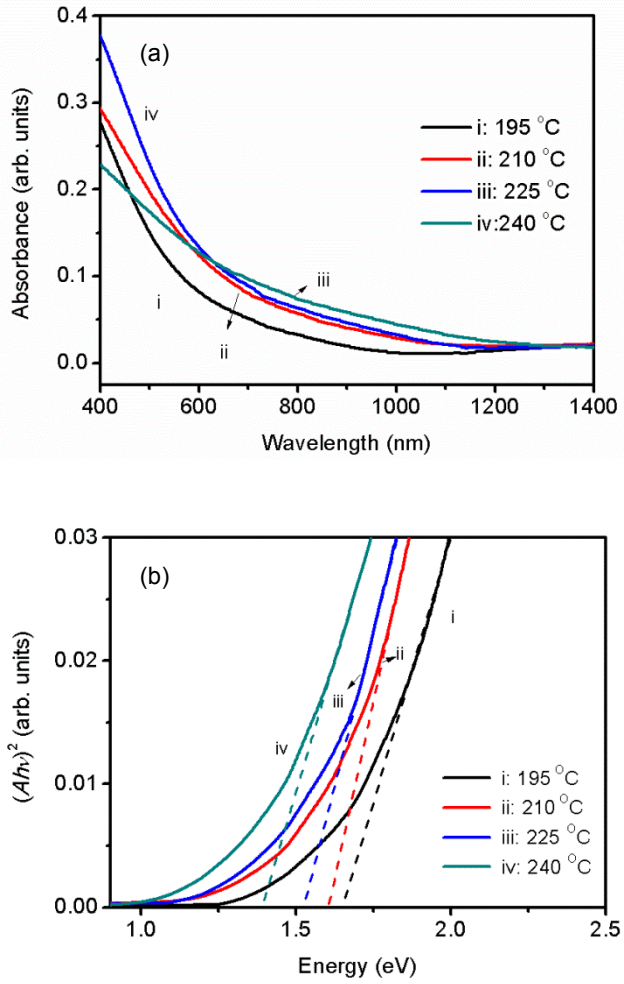

Figure 6. (a) UV-VIS-NIR absorption spectra and (b) dependence of $(Ahv)^2$ on hv of the CZTS nanocrystals prepared at different temperatures.

The absorption spectra of the CZTS nanocrystals fabricated at different temperatures are shown in figure 6 (a). It can be seen that all the samples exhibited broad absorption in the visible region. The band gaps of the CZTS nanocrystals were estimated by extrapolating the linear part of the function $(Ahv)^2$ versus energy (hv) (where A = absorbance, h = Planck's constant, and v = frequency) as shown in figure 6 (b).

The obtained band gaps are red-shifted as the reaction temperature was increased as shown in table 2. Although the average CZTS nanocrystal diameter was observed to increase as temperature increased (figure 4c), the change in the band gap is not due to quantum confinement effects. The majority of the nanocrystals are much larger than the Bohr exciton radius of CZTS, estimated to be 3 nm depending on the values reported by Persson [26]. The presence of wurtzite CZTS at lower temperature accounts for the larger band gap energy because the wurtzite-kesterite CZTS is calculated to have large band gap compared with kesterite CZTS [25]. This is experimentally confirmed by absorption measurements performed on the rapidly cooled sample (figure 5b) that was established to be wurtzite CZTS. Analysis of figure 5 (b) reveals a higher energy band gap for this sample relative to a sample which cooled naturally. For the sample fabricated at 240 ^{o}C, the presence of ternary phase CTS (which has a relatively narrow energy band gap of 1.35 eV) is likely to be the reduction in the energy band gap.

3.3 Influence of reaction time

The XRD patterns of the CZTS nanocrystals fabricated at different reaction times (15-60 min) are shown in figure 7 (a). All diffraction patterns could be indexed to kesterite phase (PDF 026-0575). No weak peaks belonging to binary phases or wurtzite CZTS were detected. As shown in table 3, the crystal domain sizes increased from 8 nm to 11 nm as the reaction time prolonged. Grain sizes of CZTS nanocrystals prepared at different times measured from AFM images (figure S3) are also given in figure 7 (b). In contrast to the temperature dependent experiments, it can be seen that the grain sizes of CZTS nanoparticles only fluctuate in a narrow region around 15 nm when the reaction time changes. This trend is also expected at other reaction temperatures. However, the CZTS nanocrystals are more polydispersed

as the standard deviation becomes larger (figure 7b) which suggest the growth of the nanoparticles follows Ostwald ripening. Raman spectra shown in figure 7 (c) were further used to confirm the structure of the CZTS nanocrystals. There is only one clear peak located at 329 cm^{-1} as shown in figure 7 (c), which can be indexed to non-stoichiometry CZTS material. No other characteristics peaks from secondary phases can be observed. Compared with figure 4 (b), there is no shift of the characteristic peak of CZTS as reaction time prolonged from 15 min to 60 min.

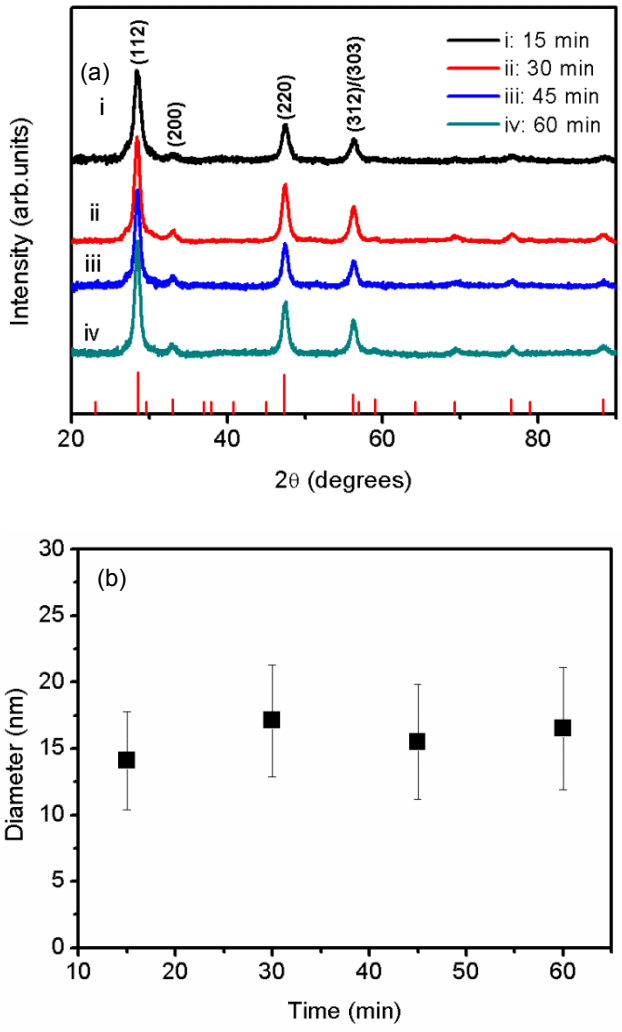

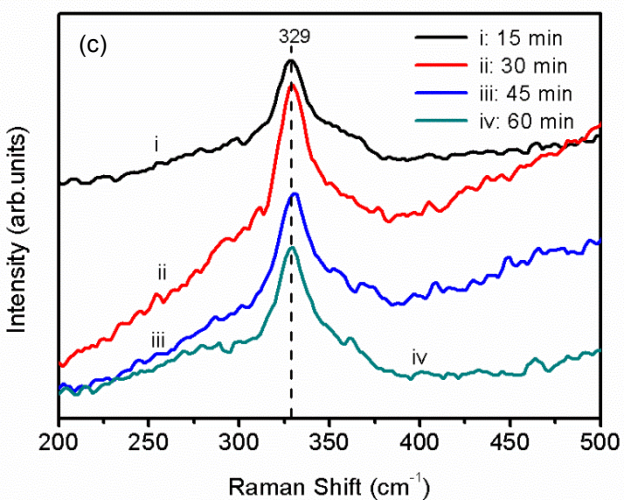

Figure 7. (a) X-ray diffraction patterns, (b) average grain sizes and (c) Raman spectra of CZTS nanocrystals prepared at a fixed temperature of 225 ^{o}C for different reaction times: (i) 15 min, (ii) 30 min, (iii) 45 min, (iv) 60 min. The red lines are the reference XRD pattern of CZTS (PDF 026-0575). Diffraction patterns and Raman spectra are off-set vertically for better visibility. The Raman spectra were smoothed using a Savitzky-Golay method.

Table 3. XRD peak intensity, calculated crystal domain size, characteristic Raman peak and band gap energy of CZTS nanocrystals fabricated at different reaction times.

sample	peak intensity		crystal size	raman peak	band gap
	(112)	220	(nm)	(cm^{-1})	(eV)
15 min	1453	596	7.9	329	1.42
30 min	1699	954	10.0	329	1.52
45 min	1537	683	10.4	329	1.62
60 min	1830	855	11.0	329	1.84

Table 4. Elemental ratios of CZTS nanocrystals fabricated at different times according to EDS measurements.

time (min)	Cu/Zn/Sn/S	Cu/(Zn+Sn)	Zn/Sn
15	2.12/0.96/1.00/4	1.08	0.96
30	1.72/1.13/0.96/4	0.83	1.18
45	1.61/1.15/0.90/4	0.79	1.27
60	1.77/1.28/0.99/4	0.78	1.28

The average composition, Cu/(Zn+Sn) and Zn/Sn, of the CZTS nanocrytals prepared at different times are summarized in table 4. The composition position on the quasi-ternary diagram of the nanocrystals is also presented in figure 3. It can be seen that nanocrystals fabricated for 30, 45 and 60 min fall in or just outside the composition region suitable for high efficiency solar cells. When the reaction time was 15 min, the composition of nanocrystals lies in the copper rich and zinc poor region. When the reaction time increases, the compositions of nanoparticles move into the copper poor and zinc rich region with the composition of tin remaining constant at the stoichiometric ratio of 0.25.

The composition of the nanocrystals as a function of time can be explained by considering the hard-soft acid-base theory [27]. Cu^{+} is a soft Lewis acid and is therefore the most reactive metal precursor towards the soft lewis base S^{2-}. Consequently, $Cu_{2-x}S$ is first formed at the beginning of the reaction. As the reaction time evolves, Sn^{4+} and Zn^{2+} are gradually incorporated into the crystal of $Cu_{2-x}S$ replacing Cu ions. In this case, Sn^{4+} diffuses into the $Cu_{2-x}S$ nucleus to form Cu-Sn-S compounds at the beginning of the reaction followed by the replacement of Cu^{+} with Zn^{2+} to form CZTS. This is supported by the constant composition of tin throughout the reaction progress. It is likely that Cu^{+} will be preferentially replaced with Zn^{2+} rather than Sn^{4+} because its ionic radius (77 pm) is closer to that of Zn^{2+} (74 pm). This is supported by the increasing zinc composition as the reaction time increases (figure 3).

The influence of the reaction time on the optical properties of the CZTS nanocrytals is presented in figure 8.

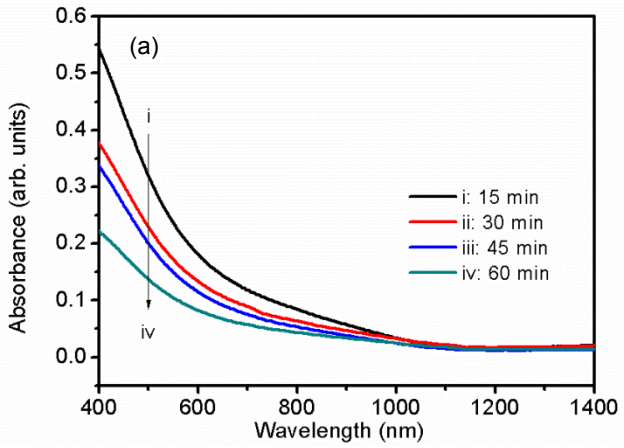

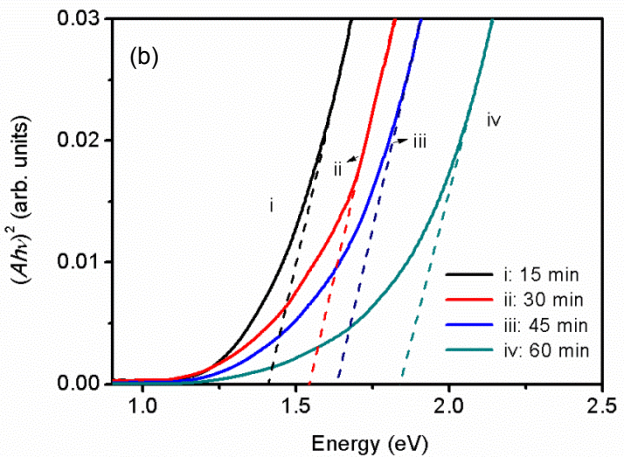

Figure 8. (a) UV-VIS-NIR absorption spectra and (b) dependence of $(Ahv)^2$ on hv of the CZTS nanocrystals prepared for different reaction times.

As in temperature-dependent experiments, all the samples exhibited broad absorption in the visible region as shown in figure 8 (a). As the reaction time increased, the absorption edge of CZTS nanocrystals gradually shifted toward shorter wavelengths. As shown in figure 8 (b), the band gaps were estimated to be 1.42, 1.52, 1.61, and 1.84 eV for CZTS nanocrystals prepared at 15, 30, 45, and 60 min, respectively. CZTS is thought to be a highly doped semiconductor [28] and it has been reported that the excess carriers result in a blue shift of the energy band gap according to the Moss-Burnstein effect [29,30]. Under Cu-poor/Zn-rich conditions, V_{Cu}^{-} and Zn_{Cu}^{+} become the dominant defects in the system [31]. As the composition of nanocrystals become poorer in copper and richer in Zn, the excess holes provided by V_{Cu}^{-} may reduce the valence band maximum and the excess electrons provided by Zn_{Cu}^{+} increase the conduction band minimum accounting for the observed increase in energy band gap with reaction time.

4. Conclusion

In summary, high quality CZTS nanocrystals have been synthesized using hot-injection of precursors. The influence of reaction temperature and time on the structural, composition and optical properties of the nanocrystals has been systematically investigated. Temperature-dependent experiments revealed that wurtzite CZTS was formed at lower temperature whereas CTS was present at higher temperature. These

factors were found to have a profound influence on the energy band gap of the nanocrystals. Time-dependent experiments showed that the band gap of as-synthesized CZTS was blue-shifted as the composition of the nanocrystals became poorer in copper and richer in zinc when reaction time increased. Analysis of the experimental data indicates that it is crucial to optimize the reaction conditions to fabricate CZTS nanocrystals in a narrow compositional region that is suitable for use in high efficiency solar cell devices.

Acknowledgments

NB and GZ gratefully acknowledge funding from the Royal Society (Research Grant R120090). The authors also thank Dr. Wenyue Li at City University of Hong Kong for performing the TEM and Raman measurements.

References

[1] Green M A, Emery K, Hishikawa Y, Warta W and Dunlop E D 2013 Solar cell efficiency tables (Version 41) *Prog. Photovoltaics: Res. Appl.* **21** 1-11

[2] Scragg J J, Dale P J, Peter L M, Zoppi G and Forbes I 2008 New routes to sustainable photovoltaics: evaluation of Cu_2ZnSnS_4 as an alternative absorber material *Phys. Status Solidi B* **245** 1772-78

[3] Riha S C, Parkinson B A and Prieto A L 2009 Solution-based synthesis and characterization of Cu_2ZnSnS_4 nanocrystals *J. Am. Chem. Soc.* **131** 12054-55

[4] Guo Q J, Hillhouse H W and Agrawal R 2009 Synthesis of Cu_2ZnSnS_4 nanocrystal ink and its use for solar cells *J. Am. Chem. Soc.* **131** 11672-73

[5] Guo Q J, Ford G M, Yang W C, Hages C J, Hillhouse H W and Agrawal R 2012 Enhancing the performance of CZTSSe solar cells with Ge alloying *Sol. Energy Mater. Sol. Cells* **105** 132-6

[6] Steinhagen C, Panthani M G, Akhavan V, Goodfellow B, Koo B and Korgel B 2009 A Synthesis of Cu_2ZnSnS_4 nanocrystals for use in low-cost photovoltaics *J. Am. Chem. Soc.* **131** 12554-5

[7] Zoppi G, Forbes I, Miles R W, Dale P J, Scragg J J and Peter L M 2009 $Cu_2ZnSnSe_4$ thin film solar cells produced by selenisation of magnetron sputtered precursors *Prog. Photovoltaics: Res. Appl.* **17** 315-9

[8] Todorov T K, Reuter K B and Mitzi D B 2010 High-efficiency solar cell with earth-abundant liquid-processed absorber *Adv. Mater.* **22** E156-9

[9] Ahmed S, Reuter K B, Gunawan O, Guo L, Romankiw L T and Deligianni H 2012 A high efficiency electrodeposited Cu_2ZnSnS_4 solar cell *Adv. Energy Mater.* **2** 253-9

[10] Zhou H, Song T B, Hsu W C, Luo S, Ye S, Duan H S, Hsu C J, Yang W and Yang Y 2013 Rational defect passivation of $Cu_2ZnSn(S,Se)_4$ photovoltaics with solution-processed Cu_2ZnSnS_4:Na nanocrystals. *J. Am. Chem. Soc.* **135** 15998-16001

[11] Miskin C K, Yang W C, Hages C J, Carter N J, Joglekar C S, Stach E A and Agrawal R 2014 9.0% efficient $Cu_2ZnSn(S,Se)_4$ solar cells from selenized nanoparticle inks. *Prog. Photovoltaics: Res. Appl.* DOI: 10.1002/pip.2472

[12] Tan J M R, Lee Y H, Pedireddy S, Baikie T, Ling X Y and Wong L H 2014 Understanding the synthetic pathway of a single-phase quarternary semiconductor using surface-enhanced Raman scattering: a case of wurtzite Cu_2ZnSnS_4 nanoparticles *J Am. Chem. Soc.* **136** 6684-92

[13] Fernandes P A, Salomé P M P and da Cunha A F 2011 Study of polycrystalline Cu_2ZnSnS_4 films by Raman scattering. *J. Alloy. Comp.* **509** 7600-6

[14] Zou Y, Su X and Jiang J 2013 Phase-controlled synthesis of Cu_2ZnSnS_4 anocrystals: the role of reactivity between Zn and S *J. Am. Chem. Soc.* **135** 18377-84

[15] Li M, Zhou W H, Guo J, Zhou Y L, Hou Z L Jiao J, Zhou Z J, Du Z L and Wu S X 2012 Synthesis of pure metastable wurtzite CZTS nanocrystals by facile one-Pot method *J. Phys. Chem. C* **116** 26507-16.

[16] Xu J, Yang X, Yang Q D, Wong T L and Lee C S 2012 Cu_2ZnSnS_4 hierarchical microspheres as an effective counter electrode material for quantum dot sensitized solar cells *J. Phys. Chem. C* **116** 19718-23.

[17] Suehiro S, Horita K, Kumamoto K, Yuasa M, Tanaka T, Fujita K, Shimanoe K and Kida T 2013 Solution-processed Cu_2ZnSnS_4 nanocrystal solar cells: efficient stripping of surface insulating layers using alkylating agents *J. Phys. Chem. C* **118** 804-10

[18] Carrete A, Shavel A, Fontané X, Montserrat J, Fan J, Ibáñez M, Saucedo E, Pérez-Rodríguez A and Cabot A 2013 Antimony-based ligand exchange to promote crystallization in spray-deposited $Cu_2ZnSnSe_4$ solar cells. *J. Am. Chem. Soc.* **135** 15982-5

[19] Zhou Y L, Zhou W H, Li M, Du Y F and Wu S X 2011 Hierarchical Cu_2ZnSnS_4 particles for a low-cost solar cell: morphology control and growth mechanism *J. Phys.Chem. C* **115** 19632-9

[20] Caballero R, Garcia-Llamas E, Merino J M, León M, Babichuk I, Dzhagan V, Strelchuk V and Valakh M 2014 Non-stoichiometry effect and disorder in Cu_2ZnSnS_4 thin films obtained by flash evaporation: Raman scattering investigation. *Acta Mater.* **65** 412-7

[21] Lu X, Zhuang Z, Peng Q and Li Y 2011 Wurtzite Cu_2ZnSnS_4 nanocrystals: a novel quaternary semiconductor *Chem. Commun.* **47** 3141-3

[22] Yang W C, Miskin C K, Hages C J, Hanley E C, Handwerker C, Stach E A and Agrawal R 2014 Kesterite $Cu_2ZnSn(S,Se)_4$ absorbers converted from metastable, wurtzite-derived Cu_2ZnSnS_4 nanoparticles *Chem. Mater.* **26** 3530-4

[23] Fang X, Zhai T, Gautam U K, Li L, Wu L, Bando Y and Golberg D 2011 ZnS nanostructures: from synthesis to applications. *Prog. Mater. Sci.* **56** 175-287

[24] Cao M and Shen Y 2011 A mild solvothermal oute to kesterite quaternary Cu_2ZnSnS_4 nanoparticles *J. Cryst. Growth* **318** 1117-20

[25] Chen S, Walsh A, Luo Y, Yang J H, Gong X G and Wei S H 2010 Wurtzite-derived polytypes of kesterite and stannite quaternary chalcogenide semiconductors *Phys. Rev. B* **82** 195203

[26] Persson C 2010 Electronic and optical properties of Cu_2ZnSnS_4 and $Cu_2ZnSnSe_4$ *J. Appl. Phys.* **107** 053710

[27] Pearson R G 1963 Hard and soft acids and bases *J. Am. Chem. Soc.* **85** 3533-9

[28] Leitão J P, Santos N M, Fernandes P A, Salomé P M P, da Cunha A F, González J C, Ribeiro G M and Matinaga F M 2011 Photoluminescence and electrical study of fluctuating potentials in Cu_2ZnSnS_4-based thin films *Phys. Rev. B* **84** 024120

[29] Burstein E 1954 Anomalous optical absorption limit in InSb *Phys. Rev.* **93** 632-3

[30] Tanaka K, Fukui Y, Moritake N and Uchiki H 2011 Chemical composition dependence of morphological and optical properties of Cu_2ZnSnS_4 thin films deposited by sol–gel sulfurization and Cu_2ZnSnS_4 thin film solar cell efficiency *Sol. Energy Mater. Sol. Cells* **95** 838-42

[31] Chen S, Gong X G Walsh A and Wei S H 2010 Defect physics of the kesterite thin-film solar cell absorber Cu_2ZnSnS_4 *Appl. Phys. Lett.* **96** 021902